

Topochemical Deintercalation of Li from Layered LiNiB: toward 2D MBene

Gourab Bhaskar, Volodymyr Gvozdetskyi, Maria Batuk, Kamila M. Wiaderek, Yang Sun, Renhai Wang, Chao Zhang, Scott L. Carnahan, Xun Wu, Raquel A. Ribeiro, Sergey L. Bud'ko, Paul C. Canfield, Wenyu Huang, Aaron J. Rossini, Cai-Zhuang Wang, Kai-Ming Ho, Joke Hadermann, and Julia V. Zaikina*



Cite This: *J. Am. Chem. Soc.* 2021, 143, 4213–4223



Read Online

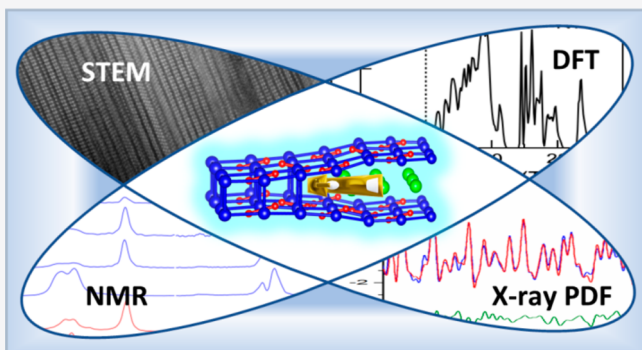
ACCESS |

Metrics & More

Article Recommendations

Supporting Information

ABSTRACT: The pursuit of two-dimensional (2D) borides, MBenes, has proven to be challenging, not the least because of the lack of a suitable precursor prone to the deintercalation. Here, we studied room-temperature topochemical deintercalation of lithium from the layered polymorphs of the LiNiB compound with a considerable amount of Li stored in between [NiB] layers (33 at. % Li). Deintercalation of Li leads to novel metastable borides ($\text{Li}_{\sim 0.5}\text{NiB}$) with unique crystal structures. Partial removal of Li is accomplished by exposing the parent phases to air, water, or dilute HCl under ambient conditions. Scanning transmission electron microscopy and solid-state ^7Li and ^{11}B NMR spectroscopy, combined with X-ray pair distribution function (PDF) analysis and DFT calculations, were utilized to elucidate the novel structures of $\text{Li}_{\sim 0.5}\text{NiB}$ and the mechanism of Li-deintercalation. We have shown that the deintercalation of Li proceeds via a “zip-lock” mechanism, leading to the condensation of single [NiB] layers into double or triple layers bound via covalent bonds, resulting in structural fragments with $\text{Li}[\text{NiB}]_2$ and $\text{Li}[\text{NiB}]_3$ compositions. The crystal structure of $\text{Li}_{\sim 0.5}\text{NiB}$ is best described as an intergrowth of the ordered single [NiB], double [NiB]₂, or triple [NiB]₃ layers alternating with single Li layers; this explains its structural complexity. The formation of double or triple [NiB] layers induces a change in the magnetic behavior from temperature-independent paramagnets in the parent LiNiB compounds to the spin-glassiness in the deintercalated $\text{Li}_{\sim 0.5}\text{NiB}$ counterparts. LiNiB compounds showcase the potential to access a plethora of unique materials, including 2D MBenes (NiB).



INTRODUCTION

An understanding of the reversible Li-ion intercalation-deintercalation mechanism, driven by electrochemical forces, has tremendously advanced the field of electrical energy storage and shaped modern society.^{1–3} Another area where (de)intercalation processes play substantial roles is in the synthesis of 2D materials.^{4–10} *Chimie douce* (soft chemistry) methods allow for the preparation of 2D materials under mild conditions in the course of topochemical deintercalation reactions.^{11–14} Unlike conventional solid-state high-temperature syntheses, oftentimes resulting in thermodynamically stable products, topochemical deintercalation may yield metastable phases that are otherwise inaccessible. Topochemical reactions involve the elimination of “guest” entities from the “host” frameworks, thus deintercalated products often maintain structural features of the “host”. As the structural changes are minimal, the need for the use of extreme synthesis conditions (e.g., elevated temperature) is superfluous.

Examples of metastable compounds that can only be obtained by topochemical deintercalation are layered VS_2 ,

$\text{Co}(\text{S}, \text{Se})$, and $\text{Na}_{1-y}\text{Fe}_{2-x}\text{As}_2$ prepared via oxidative deintercalation of alkali metals from LiVS_2 ,¹⁵ $\text{K}_{1-x}\text{Co}_2(\text{S}, \text{Se})_2$,¹⁶ and NaFeAs ,^{17–19} respectively. By tuning of the reaction conditions, a controlled deintercalation of K from the KNi_2Se_2 compound leads to $\text{K}_{1-x}\text{Ni}_2\text{Se}_2$, $\text{K}_{1-y}\text{Ni}_{2-z}\text{Se}_2$, and finally, Ni_3Se_4 .²⁰ Topochemical deintercalation expanded Ge allotropes’ family since metastable forms with 3D porous structures can only be accessed by alkali metal’s deintercalation from binary $\text{Li}_7\text{Ge}_{12}$ and $\text{Na}_{12}\text{Ge}_{17}$ phases.^{21–24} Similarly, Ge and Si analogs of graphene, germanene and a layered polysilane, were prepared by topotactic deintercalation of Ca^{2+} from $\beta\text{-CaGe}_2$ ⁴ and CaSi_2 ^{25,26} under mild reaction

Received: October 30, 2020

Published: March 15, 2021



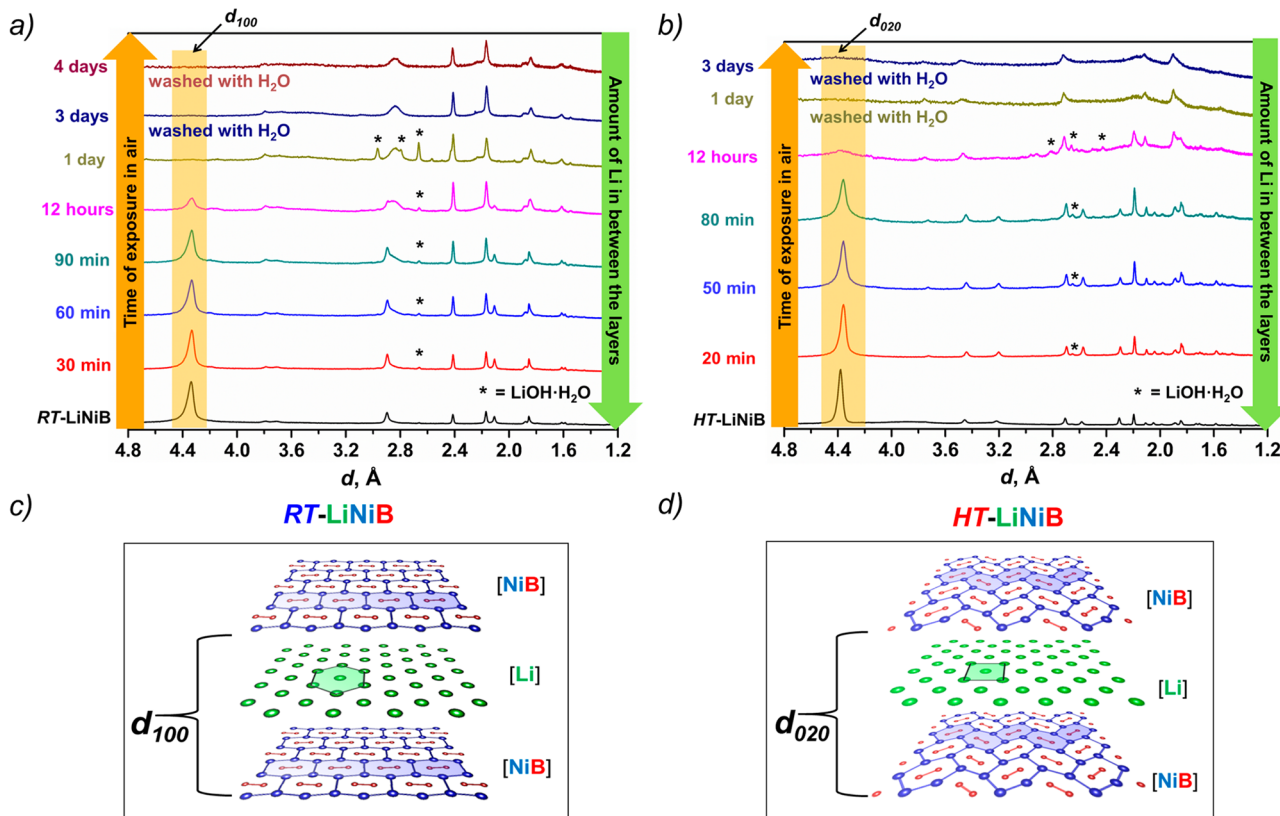


Figure 1. Powder X-ray diffraction patterns of *RT*-LiNiB (a) and *HT*-LiNiB (b) exposed to air. The content of LiOH·H₂O (characteristic peaks marked with *) is increasing while intensities of Bragg peaks with (100) and (020) $h\bar{k}l$ for both polymorphs are decreasing with time. Crystal structures of *RT*(*m*)-LiNiB (c) and *HT*-LiNiB (d) compounds built from alternating Li- and [NiB]-layers.

conditions. The versatility of precursors and reaction media, as well as mild synthesis conditions, makes topochemical deintercalation a potent tool to synthesize a variety of multifunctional materials that are inaccessible by traditional solid-state methods.

Topochemical deintercalation allows preparation of 2D layered carbides, $M_{n+1}X_n$ from the parent $M_{n+1}AX_n$ (MAX) phases, where M = early transition metal, A = elements of groups 13–14 (mainly Al or Si), and X = C or N.^{27,28} The term MXene is coined for these 2D compounds which are analogous to 2D graphene. Benefiting from the stronger M-X bonds compared to the M-A bonds in MAX phases, A atoms can be selectively etched under mild reaction conditions, leading to 2D $M_{n+1}X_n$ multilayers with structures identical to the parent MAX phases. For instance, synthesis of 2D Ti₃C₂ was achieved by topochemical deintercalation of Al from layered Ti₃AlC₂.^{29,30} Similar to graphene, MXenes have been suggested as materials for various applications: sensors and biosensors;³¹ printed and patterned coatings for device applications;³² supercapacitors;³³ Li, Na, K-ion batteries;^{34–37} energy storage;³⁸ piezoresistive sensors;³⁹ and catalysts.⁴⁰

Attempts have been made for the synthesis of boron analogs of 2D MXene, namely, MBene: deintercalation of In from layered Ti₂InB₂⁴¹ and Al from MoAlB,^{42,43} however, bulk preparation of MBene is still challenging which is evident from the scarcity of reports about MBenes in contrast to those about MXenes. On the contrary, theoretical calculations suggest a plethora of applications for 2D MBenes^{44,45} in magnetic devices,⁴⁶ electrocatalysis,⁴⁷ and battery applications⁴⁸ thus

making the exploration of these classes of compounds promising.

Recently, we reported a novel compound LiNiB, which exists as two polymorphs: room-temperature *RT*-LiNiB and its high-temperature sibling *HT*-LiNiB.⁴⁹ The alternating [NiB] and Li layers (Figure 1, Figure S1) make their structural motif unique among the metal borides. Unique layered structures for both LiNiB polymorphs with a considerable amount of Li stored in between [NiB] layers (33 at. % Li) call for the detailed investigation of the Li deintercalation, in particular, with the goal of accessing isolated sheets of 2D MBenes. Here, we focus on the evolution of layered [Ni-B] frameworks in the parent LiNiB phases upon Li deintercalation during topochemical reactions in different chemical environments. We show that by controlling reaction conditions, Li can be partially removed, leading to metastable phases with an approximate composition of Li_{~0.5}NiB in which different fragments of the parent structure, i.e., Li[NiB], Li[NiB]₂, or Li[NiB]₃, can be stabilized. We have studied the atomic structure of Li_{~0.5}NiB by the synergistic trio of scanning transmission electron microscopy (STEM), X-ray pair distribution function (PDF) analysis, and density functional theory (DFT) calculations, presenting a novel methodology to structurally characterize 2D metastable materials. Lastly, we established that Li deintercalation induces a change in magnetic property from paramagnetism to spin glassiness.

EXPERIMENTAL SECTION

LiNiB precursors were synthesized via a high-temperature reaction of LiH, Ni, and B powders.⁴⁹ Deintercalation of Li from both *RT*- and

HT-LiNiB phases were carried out in air and in various solvents, such as deionized water, ethanol, and 10% v/v HCl at room temperature. Reactions in the solvents were performed under an inert atmosphere, either in a Schlenk line under argon flow or in an argon-filled glovebox. All samples were characterized via laboratory powder X-ray diffraction (PXRD) using Rigaku MiniFlex600 powder diffractometer with Cu $\text{K}\alpha$ radiation ($\lambda = 1.54051 \text{ \AA}$). Selected samples of products of deintercalation were characterized via high angle annular dark field scanning transmission electron microscopy (HAADF STEM) and electron energy-loss spectroscopy (STEM-EELS) using a probe aberration-corrected FEI Titan 80–300 “cubed” microscope operated at 300 kV. Additionally, the elemental analysis was performed via energy-dispersive X-ray spectroscopy (EDXS) and inductively coupled plasma mass spectrometry (ICP-MS). Solid state ^7Li and ^{11}B NMR spectra were measured on a Bruker widebore 9.4 T (400 MHz) NMR spectrometer equipped with an Avance III HD console. A 2.5 mm probe and a 25 kHz magic angle spinning frequency were used in all cases. Room-temperature high resolution synchrotron powder diffraction and total scattering data suitable for PDF analysis were collected at beamlines 11-BM ($\lambda = 0.412749 \text{ \AA}$) and 17-BM ($\lambda = 0.24156 \text{ \AA}$), respectively, in Advanced Photon Source (APS), Argonne National Laboratory. Magnetic property measurements were done on the polycrystalline samples using a Quantum Design MPMS XL and MPMS3 SQUID magnetometers. First-principles calculations were carried out using density functional theory (DFT) within a generalized gradient approximation (GGA) by VASP code. The calculations of phonon density of states were performed using the finite displacement with the supercell approach provided by the Phonopy code. Further details of synthesis and characterization methods used can be found in the Supporting Information.

RESULTS AND DISCUSSION

The crystal structures of *RT*-LiNiB and *HT*-LiNiB phases feature alternating [NiB] and Li layers, but the topologies of both layers are different in the two polymorphs (Figure 1, Figure S1). High resolution synchrotron powder X-ray diffraction data revealed additional structural complexity of *RT*-LiNiB manifested in the intergrowth of different stacking sequences of [NiB] layers.⁴⁹ Powder X-ray diffraction patterns for both *RT*- and *HT*-LiNiB polymorphs have the most intensive characteristic peak at $d \sim 4.4 \text{ \AA}$, corresponding to the interlayer distance between adjacent [NiB] layers. For the study of deintercalation of Li from *RT*- and *HT*-LiNiB compounds in air, powder X-ray diffraction (PXRD) data were collected over a variable time scale to monitor structural changes. As evident from Figure 1a, the intensity of the peak at $d \sim 4.4 \text{ \AA}$ (pale orange region) gradually decreases with exposure time, while the relative intensities of most of the other peaks increase. Simultaneously, intensities of new peaks in the $d \sim 3.0$ – 2.2 \AA range, identified as $\text{LiOH} \cdot \text{H}_2\text{O}$, increase with time. This is indicative of the deintercalation of Li from the layers through the reaction with $\text{O}_2/\text{H}_2\text{O}$ in air. After the *RT*-LiNiB sample was exposed to air for 24 h, the intensity of the $d \sim 4.4 \text{ \AA}$ peak vanished. After washing the sample with deionized water, the pH of the filtrate was basic due to the dissolution of LiOH. No observable changes in the PXRD pattern were detected upon exposure to air for longer than 24 h (tests were performed for up to one month). Similar gradual changes in the PXRD patterns were also observed in the case of the *HT*-LiNiB phase (Figure 1b).

For a further understanding of the Li-deintercalation mechanism, both *RT*- and *HT*-LiNiB compounds were exposed in anaerobic conditions to water, ethanol, and 10% v/v HCl. After water was added to both compounds, the pH of the solution was basic in both cases due to the formation of LiOH. We noticed that the Li-deintercalation process is slower

in these solvents than in air. For example, in the case of *RT*-LiNiB, even after 30 days of exposure to water, the peak at $d \sim 4.4 \text{ \AA}$ did not disappear completely (Figure S2). In ethanol, the deintercalation rate is faster than that in water, as the intensity of the $d \sim 4.4 \text{ \AA}$ peak decreased significantly within 3 days of exposure. Similarly, the rate of deintercalation is found to be faster in ethanol than in water in the case of *HT*-LiNiB (Figure S2). Deintercalation in 10% V/V HCl (Figures S2, S3) proceeds at a remarkably slower rate than in air.

Overall, the broadening of the PXRD peaks for the deintercalated products suggests their lower crystallinity as compared to that of the parent LiNiB compounds. That is especially pronounced in the case of Li-deintercalated *HT*-LiNiB. Energy dispersive X-ray analysis (EDX) confirmed the presence of only Ni and B in both deintercalated products; however, this method cannot detect Li. Scanning electron microscopy (SEM) images revealed the plate-like morphology of crystallites (Figure S4), suggesting that layered structure is preserved after Li deintercalation. Comparison of X-ray powder diffraction patterns of *RT*-LiNiB and its Li-deintercalated product, *RT*- $\text{Li}_{1-\gamma}\text{NiB}$, suggests that the structure of the [NiB] layer is preserved to some extent, although the deintercalation cannot be understood by a trivial shrinking of the interlayer distance (Figure S5).

We utilized high angle annular dark field (HAADF) scanning transmission electron microscopy (STEM) to shed light on the structural features of the Li-deintercalated products from both *RT*- and *HT*-LiNiB compounds. In a HAADF-STEM image, the intensity is approximately proportional to the square of the atomic number, thus heavy atoms (in this case Ni) appear bright, and light atoms such as Li and B cannot be seen at all. A HAADF-STEM image of Li-deintercalated *RT*-LiNiB (Figure 2) revealed that the layered morphology of the parent structure is preserved, while Li is partially removed from the interlayer spacing. As it will be shown below, Li content was determined by a comprehensive set of characterization techniques to be ~ 0.6 for the deintercalated product formed from *RT*-LiNiB and ~ 0.4 for the deintercalated product formed from *HT*-LiNiB. For the sake of clarity, the deintercalated compounds are referred to as *RT*- $\text{Li}_{0.6}\text{NiB}$ and *HT*- $\text{Li}_{0.4}\text{NiB}$ hereafter. HAADF-STEM images of *RT*- $\text{Li}_{0.6}\text{NiB}$ show that there are several different orderings of the [NiB] layers present. Three different substructures are labeled as *RT*-A, *RT*-B, and *RT*-C. *RT*-A fragment is the parent structure where every Li layer is alternating with [NiB] monolayer, whereas in the substructures *RT*-B and *RT*-C, the Li layer is alternating with doubled or tripled [NiB] layers, respectively, e.g., $\text{Li}[\text{NiB}]_2$ or $\text{Li}[\text{NiB}]_3$. Interestingly, substructures with more than 3 stacking [NiB] layers are not detected. As it can be seen from Figure 2, the *RT*-A, *RT*-B, and *RT*-C substructures are randomly distributed along the stacking direction with substructure *RT*-B or $\text{Li}[\text{NiB}]_2$ statistically being more abundant than *RT*-A and *RT*-C. Noticeably, removing one Li layer does not cause a relative shift between the two condensed [NiB] layers within the *RT*-B substructure. Conversely, removing the second adjacent Li layer entails a relative shift of the [NiB] layers within the *RT*-C $\text{Li}[\text{NiB}]_3$ substructure. The [NiB] layers in *RT*-C are not stacked linearly: one of the layers is shifted compared to the other two from the $[\text{NiB}]_3$ fragment. After the first Li layer is removed, four different orientations of the same unit cell can occur depending on which of the Li layers is removed next (Figure S6). All of these orientations can be seen

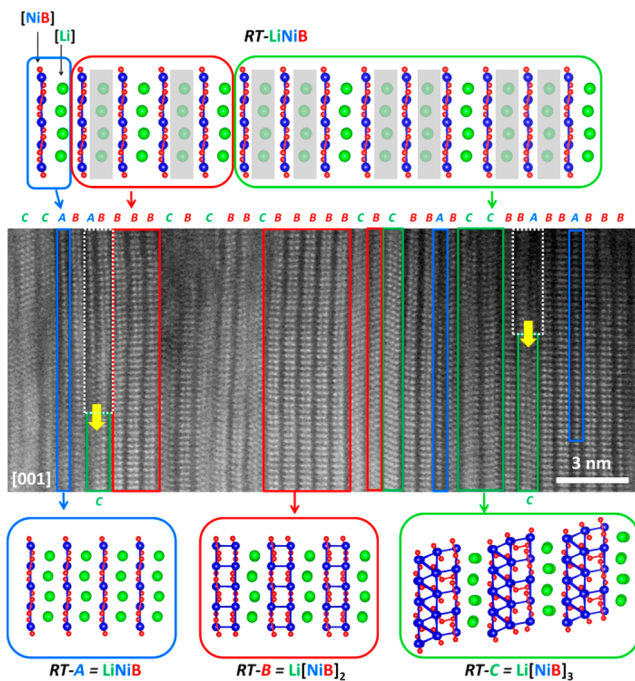


Figure 2. HAADF-STEM image of $RT\text{-Li}_{0.6}\text{NiB}$ showing a random distribution of three types of substructures: $RT\text{-A}$ ($\text{Li}[\text{NiB}]$), $RT\text{-B}$ ($\text{Li}[\text{NiB}]_2$), and $RT\text{-C}$ ($\text{Li}[\text{NiB}]_3$). The viewing zone axis is $[001]$ with respect to the parent structure. Substructure $RT\text{-A}$ resembles the parent structure $\text{Li}[\text{NiB}]$. Substructure $RT\text{-B}$ is formed by deintercalation of every other Li layer from the parent structure, so $\text{Li}[\text{NiB}]_2$ with doubled $[\text{NiB}]$ layers is formed. Similarly, to form substructure $RT\text{-C}$ $\text{Li}[\text{NiB}]_3$, every two adjacent Li layers are removed, while $[\text{NiB}]$ layers stack with a relative shift (Figure S6). “Snapshot” of the “zip-lock” Li deintercalation mechanism is highlighted by a yellow arrow demonstrating that substructure $RT\text{-C}$ (green rectangle) can be stabilized when an additional Li layer is removed from the adjacent $RT\text{-A}$ and $RT\text{-B}$ substructures (white rectangular). Green/red/blue boxes do not represent the crystallographic unit cells of the substructures but rather highlight the structural motifs.

in the different regions of the STEM image (Figure S6). Reorganization of the $[\text{NiB}]$ layers in the $RT\text{-C}$ substructure also affects the neighboring substructures by enforcing a certain shift/deformation within their layers. This induced shift is most prominent when $RT\text{-B}$ fragment is surrounded by $RT\text{-C}$ fragments (Figure S6).

Assuming that the absence of contrast between the Ni columns is equivalent to Li layers (Li and B atoms cannot be seen in HAADF-STEM) and taking into account the ratio between the numbers of Li layers and numbers of $[\text{NiB}]$ layers in the $RT\text{-Li}_{0.6}\text{NiB}$ (i.e., 37:83 in the analyzed area), we estimated that about 55% of Li had been deintercalated from the parent compound (Figure 2). A similar average Li/Ni ratio of 0.62:1 was obtained for different areas of the sample (Figures S7, S8). Importantly, the HAADF-STEM images explain why the Li deintercalation from $RT\text{-LiNiB}$ can be monitored by the decrease in intensity of the peak with $d \sim 4.4$ Å that corresponds to the interlayer $[\text{NiB}]$ distance in $RT\text{-LiNiB}$. Even though $RT\text{-A}$ substructures with an interlayer distance of 4.4 Å, are still present in $RT\text{-Li}_{0.6}\text{NiB}$, the long-range translation symmetry is lost since $RT\text{-A}$ substructures are only scarcely present and sporadically distributed.

From the analysis of HAADF-STEM images, the average $[\text{NiB}]$ interlayer distances in $RT\text{-B}$ and $RT\text{-C}$ substructures

were estimated to be $\sim 2.2(1)$ Å and $2.1(1)$ Å, respectively (Figure S8). All three substructures are randomly distributed along the direction perpendicular to the layers, i.e., along the a -axis. HAADF-STEM images of $HT\text{-Li}_{0.4}\text{NiB}$ phase (Figure S9) also show irregular distributions of multiple stacked $[\text{NiB}]$ layers, however because of the extremely low crystallinity of the material, atomic resolution images could not be obtained.

We utilized density functional theory (DFT) calculation to assess the relative stability of the formed substructures and to determine the extent of Li deintercalation attainable. The initial models of the substructures $RT\text{-B}$ and $HT\text{-B}$ ($\text{Li}[\text{NiB}]_2$), $RT\text{-C}$ and $HT\text{-C}$ ($\text{Li}[\text{NiB}]_3$), $RT\text{-}[\text{NiB}]_\infty$ and $HT\text{-}[\text{NiB}]_\infty$ were derived from the structures of the parent $RT\text{-LiNiB}$ and $HT\text{-LiNiB}$ compounds by removing every other Li layer, every two Li layers, or all of the Li layers, respectively. Additionally, the stability of the $RT\text{-NiB}$ (2D) and $HT\text{-NiB}$ (2D) single layers is assessed. The atomic positions in all structural models were optimized by the DFT calculation so that the force on each atom is relaxed. With the deintercalation of Li atoms, the formation energy increases (Figure 3, Table S1) for both $RT\text{-}$

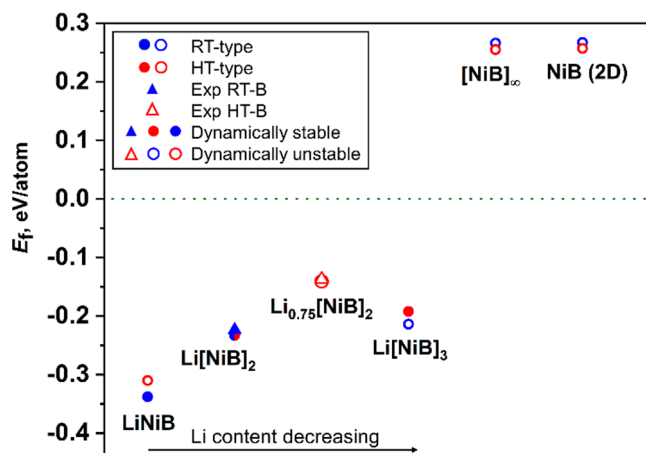


Figure 3. Formation energy (E_f) of different fragments of $RT\text{-Li}_{0.6}\text{NiB}$ and $HT\text{-Li}_{0.4}\text{NiB}$. Experimentally observed $RT\text{-B}$ and $HT\text{-B}$ substructures (see text) are marked with triangles. Filled and open symbols depict dynamically stable and dynamically unstable structures, respectively, according to computed phonon density of states.

LiNiB and $HT\text{-LiNiB}$. Fully Li-deintercalated $RT\text{-}[\text{NiB}]_\infty$ and $HT\text{-}[\text{NiB}]_\infty$ are found to be unstable with positive formation energies, indicative of their decomposition to the elemental Ni and B. However, a recent comparison between computational and experimental inorganic crystal structures suggests that predicted compounds with formation energies >0.2 eV/atom can be accessed experimentally.⁵⁰ The single layers of $RT\text{-NiB}$ (2D) and $HT\text{-NiB}$ (2D) are also found to be unstable. The partially deintercalated structures are found to be energetically stable. Their dynamical stability was further investigated by computing the phonon spectra. For RT -phase, only A ($\text{Li}[\text{NiB}]$) and B ($\text{Li}[\text{NiB}]_2$) fragments are dynamically stable, while C fragment and all fully Li-deintercalated structures become unstable with the imaginary phonon density of states (Figure S10). By analyzing the soft modes, we found the imaginary phonons in the $RT\text{-C}$ fragment are caused by the movement of Li and some of the Ni atoms along the stacking direction of layers (Figure S10). The imaginary phonons in the bulk $RT\text{-}[\text{NiB}]_\infty$ fragment are caused by the in-plane

movement of Ni and B atoms. By following the eigenvector of the soft modes in $RT\text{-}[NiB]_{\infty}$, we found that it transformed to the stable, experimentally reported NiB phase ($Cmcm$).⁵¹ In the HT fragments, only B and C models are dynamically stable (Figure S11), while fragments A and all of the fully Li-deintercalated structures become unstable. Accurate crystal structure determination of $RT\text{-Li}_{0.6}\text{NiB}$ and $HT\text{-Li}_{0.4}\text{NiB}$ from X-ray diffraction data is challenging because of the presence of light atoms (Li and B), thus only positions of heavy Ni atoms can be established, but also due to the scarcity of long-range order. As evidenced from the HAADF-STEM images, deintercalated products are composed of randomly stacked, perfectly ordered $[NiB]_n$ layers, where $n = 1, 2$, and 3 . In contrast to the traditional diffraction methods, X-ray pair distribution function (X-ray PDF) gives insight about the local order in crystalline or amorphous materials at the atomic scale. X-ray PDF is the Fourier transform of the total X-ray scattering and gives the probability of finding an atom at a certain distance from any given atom.⁵² Thus, we used PDF analysis to further understand the local atomic environment in these “semi-crystalline” materials. Similar to X-ray diffraction, X-ray PDF data for LiNiB compounds is the most informative for the interatomic distances involving Ni atoms since Ni, as the heaviest element, will dominate X-ray scattering.

We started by analyzing PDF data for the parent compounds. Both RT - and HT -LiNiB compounds are highly crystalline materials with long-range order (Figure S12). As previously established,⁴⁹ the crystal structure of RT -LiNiB can be described either as an intergrowth of two polytypes or as a superstructure (Figures 4a and S13). The best fit of the X-ray

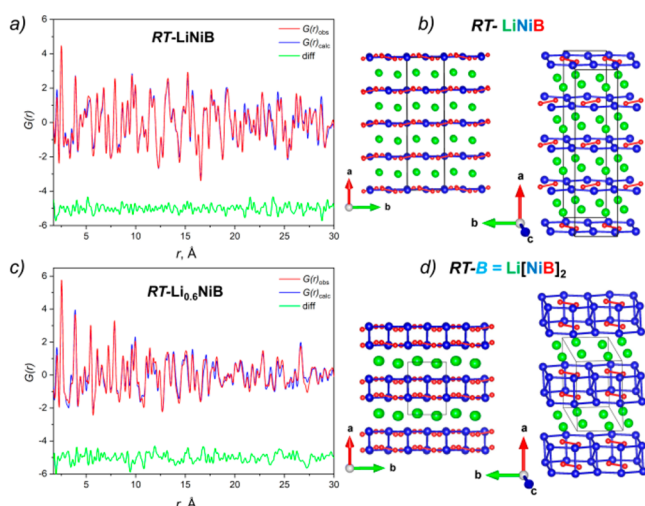


Figure 4. (a) Fitting of pair distribution function of $RT\text{-LiNiB}$, $R = 0.14$, (b) original crystal structure of $RT\text{-LiNiB}$, (c) fitting of pair distribution function of $RT\text{-Li}_{0.6}\text{NiB}$ phase, $R = 0.25$, (d) crystal structure of $RT\text{-B Li}[NiB]_2$ as determined from X-ray PDF.

PDF data was obtained for the superstructure ($P2_1/c$, supercell $4a \times b \times c$), unambiguously indicating that this is the better approximation of the real structure for the $RT\text{-LiNiB}$ compound with the complex intergrowth of $[NiB]$ layers. The X-ray PDF data fit with each of the two polytypes did not produce a sufficiently good fit (Figure S13). The $HT\text{-LiNiB}$ structure ($P2_1/m$), previously determined,⁴⁹ provides a sufficiently good fit of X-ray PDF data (Figure 5a).

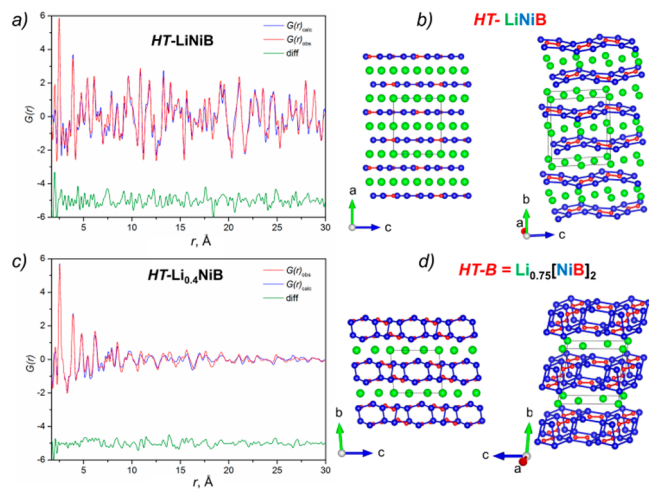


Figure 5. (a) Fitting of the pair distribution function of $HT\text{-LiNiB}$, $R = 0.27$; (b) crystal structure of $HT\text{-LiNiB}$, (c) fitting of the pair distribution function of $HT\text{-Li}_{0.4}\text{NiB}$ phase, $R = 0.26$, (d) crystal structure of $HT\text{-B Li}_{0.75}[\text{NiB}]_2$ as determined from X-ray PDF compared to the parent structure.

Upon the deintercalation of lithium, long-range order is lost, as the $RT\text{-Li}_{0.6}\text{NiB}$ compound shows moderate coherence length of the crystalline lattice up to ~ 74 Å. $HT\text{-Li}_{0.4}\text{NiB}$ exhibits only short-range order up to ~ 14 Å (~ 3 unit cells), unlike its crystalline parent structure (coherence length >100 Å) (Figure S12). Comparison of the PDF data of the parent compounds with that of their deintercalated counterparts in the short-range of 2–8 Å (Figure S14) indicates that the local coordination of Ni atoms within the $[NiB]$ layers is preserved, while most of Ni–Ni distances are elongated upon deintercalation, indicative of moderate distortion (Figure S14).

From the HAADF-STEM images, we see that the structure of $RT\text{-Li}_{0.6}\text{NiB}$ can be represented as an intergrowth of three substructures with single, double, and triple $[NiB]$ layers separated by Li atoms. Thus, to fit the X-ray PDF data of $RT\text{-Li}_{0.6}\text{NiB}$ and $HT\text{-Li}_{0.4}\text{NiB}$, a combination of all 3 substructures was used. The models of $RT\text{-B}$ and $RT\text{-C}$ substructures were optimized by DFT to obtain the relaxed structures with the minimum energy. For the fitting, Li and B coordinates were fixed to those obtained by DFT structure relaxation followed by refinement of Ni coordinates and unit cell parameters for $RT\text{-B}$. Only unit cell parameters were refined for $RT\text{-A}$ and $RT\text{-C}$. This results in the excellent fit of the experimental data (Figure 4, Table S2), confirming that B substructure with doubled $[NiB]_2$ layers is the most abundant in $RT\text{-Li}_{0.6}\text{NiB}$, 65(2)% molar fraction. Substructures A and C account for 25(1)% and 10(1)% respectively, resulting in an average composition of $Li_{0.54(1)}\text{NiB}$. This is in good agreement with the Li/Ni molar ratio determined experimentally by inductively coupled plasma mass spectrometry (ICP-MS): $Li/Ni = 0.61(2):1$ for $RT\text{-Li}_{0.6}\text{NiB}$, as well as the Li content determined from STEM data (Figures 2, S7–S8).

For the $HT\text{-Li}_{0.4}\text{NiB}$ deintercalated product, X-ray PDF data suggest a major rearrangement of the layers. A similar approach was used here: the $HT\text{-B}$ and $HT\text{-C}$ substructures were first optimized by DFT and used as initial models for the X-ray PDF refinement. However, refinement of only unit cell parameters resulted in a poor fit of the experimental data (Figure S15). Therefore, coordinates of Ni atoms were refined from the X-ray PDF data. It was further determined that the

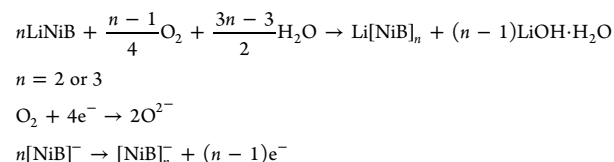
initially nearly planar [NiB] layers of the parent *HT*-LiNiB compound become corrugated upon Li deintercalation in substructure *HT*-B with the double layers, $\text{Li}[\text{NiB}]_2$, leading to large steric repulsion within the Li layer (Figure S16). Therefore, one row of atoms in the Li layer had to be removed (Figure S17), and this structure model was further optimized by DFT so that the short Li–Ni distances ($<2.3\text{ \AA}$) are absent. This results in the new model *HT*-B $\text{Li}_{0.75}[\text{NiB}]_2$, whose structure was further optimized by an iterative combination of X-ray PDF-analysis to refine unit cell parameters and Ni coordinates and DFT to optimize B and Li coordinates. After several iterative cycles of $\text{DFT} \leftrightarrow \text{X-ray PDF}$, the optimized structure of *HT*-B $\text{Li}_{0.75}[\text{NiB}]_2$ was determined (Figure 4, Table S3) whose formation energy, $E_f = -0.137\text{ eV/atom}$, is of the same magnitude as compared to the theoretically predicted *HT*-B $\text{Li}_{0.75}[\text{NiB}]_2$ with $E_f(\text{relaxed}) = -0.141\text{ eV/atom}$ (Figure 3), albeit it is dynamically unstable based on the phonon density calculations (Figure S11). This refinement confirmed that in the *HT*- $\text{Li}_{0.4}\text{NiB}$ deintercalated product, similar to *RT*- $\text{Li}_{0.6}\text{NiB}$, the *HT*-B substructure or $\text{Li}_{0.75}[\text{NiB}]_2$ is prevalent with a 90(2)% molar fraction. Molar fractions for fragments *HT*-A and *HT*-C amount to 5(1)% and 5(1)%, respectively, resulting in the average composition $\text{Li}_{0.39(1)}\text{NiB}$. This Li/Ni ratio is in excellent agreement with that obtained by inductively coupled plasma mass spectrometry (ICP-MS), $\text{Li}/\text{Ni} = 0.41(1):1$. ICP-MS was also utilized to quantify the extent of Li-deintercalation by tuning the exposure time of both *RT*-LiNiB and *HT*-LiNiB compounds in air. Analysis of the ICP-MS data, collected for samples of both compounds exposed to air for 3 h and 9 h (Figure S18), indicates gradual deintercalation of Li from the parent LiNiB compounds.

Such a comprehensive study using synergistic techniques, HAADF-STEM, DFT, and X-ray PDF, allowed us to establish a clear-cut picture of the Li deintercalation from LiNiB polymorphs. Only $\sim 50\%$ of Li atoms can be removed from the layered structures under ambient conditions. The deintercalation process follows the irreversible “zip-lock” mechanism where Li is removed layer by layer. Once a single Li layer is deintercalated, the “zip-lock” is closed as two adjacent [NiB] layers condense into thicker layers, $[\text{NiB}]_2$ or $[\text{NiB}]_3$. Most likely, this makes the reverse process, e.g., insertion of Li-layer in between [NiB] layers, extremely difficult. “Snapshot” of the “zip-lock” mechanism is highlighted in Figure 2; when *RT*-A and *RT*-B substructures (white rectangle) stack, the substructure *RT*-C (green rectangle) forms. In the case of *RT*- $\text{Li}_{0.6}\text{NiB}$ (substructure *RT*-B), the condensed [NiB] layers are nearly flat and aligned on top of each other as only new Ni–Ni bonds form with a distance of 2.58 or 2.61 \AA , which is comparable to that in Ni metal (Table S4). In the case of *HT*- $\text{Li}_{0.4}\text{NiB}$ (substructure *HT*-B), the layer becomes corrugated with some of the Ni and B atoms moving out of the layer, but the condensation of monatomic [NiB] layers into $[\text{NiB}]_2$ also proceeds through the formation of new Ni–Ni bonds in the range of 2.65 or 2.71 \AA (Table S5).

The deintercalation mechanism in LiNiB is drastically different from that for MoAlB, another layered boride,^{42,43} which is considered as a candidate for the preparation of single layer boride MBenes. In the structure of MoAlB, the $[\text{Mo}_2\text{B}_2]$ layers alternate with the zigzag double layers of Al. Upon etching with NaOH, Al is partially deintercalated, thus some of Al double layers become single layers, while the transition metal-containing layers $[\text{Mo}_2\text{B}_2]$ remain unchanged. The

resulting deintercalated product $\text{Mo}_x\text{Al}_{x-1}\text{B}_x$ with $x = 2, 3, 4$, 5 is an intergrowth of nanoscale domains of various $[\text{Mo}_2\text{B}_2] - [\text{Al}]_1$ or $[\text{Al}]_2$ stacking motifs. In turn, in LiNiB, the single [NiB] layer changed to double $[\text{NiB}]_2$ or triple $[\text{NiB}]_3$ layers upon Li deintercalation, leading to the formation of new Ni–Ni bonds.

Bader charge analysis^{53,54} of LiNiB compounds⁴⁹ showed that more electropositive Li atoms donate electrons to the [NiB]_n layer, resulting in ionic interaction between layers $\text{Li}^{+0.84}[\text{Ni}^{-0.32}\text{B}^{-0.52}]$ or simply $\text{Li}^+[\text{NiB}]^-$. Taking into account the established deintercalation mechanism and remarkably higher reactivity of LiNiB in air compared to that in water or HCl, we propose that deintercalation of Li occurs via red-ox reactions in the presence of oxidizing agent (e.g., atmospheric oxygen). Deintercalated Li cations form lithium oxide, which, in the presence of moisture, is further transformed to $\text{LiOH}\cdot\text{H}_2\text{O}$, experimentally observed in PXRD (Figure 1).



Similar charge transfer from electropositive Li to [NiB]_n layers in the deintercalated compounds *RT*- $\text{Li}_{0.6}\text{NiB}$ and *HT*- $\text{Li}_{0.4}\text{NiB}$ is suggestive from the Bader charge analysis: $\text{Li}^{+0.82}[\text{Ni}^{-0.16}\text{B}^{-0.25}]_2$ (Table S6). Bader charge analysis also suggests that upon Li deintercalation and condensation of monatomic NiB layers into $[\text{NiB}]_2$, both Ni and B are being oxidized since their formal charges increase from -0.32 to -0.16 for Ni and from -0.52 to -0.25 for B. Interestingly, for the $[\text{NiB}]_3$ substructure, Bader charge analysis suggests similar charge transfer from Ni and B to Li but only for the NiB layers adjacent to Li layer, while Ni is positively charged in the middle NiB layer of C-fragments



Solid-state NMR Spectroscopy. ⁷Li and ¹¹B magic angle spinning (MAS) solid state NMR spectra of *RT*- $\text{Li}_{0.6}\text{NiB}$ and *HT*- $\text{Li}_{0.4}\text{NiB}$ phases were acquired to shed light on the evolution of Li and B coordination environments upon deintercalation. The MAS ⁷Li NMR spectrum (Figure 6) of

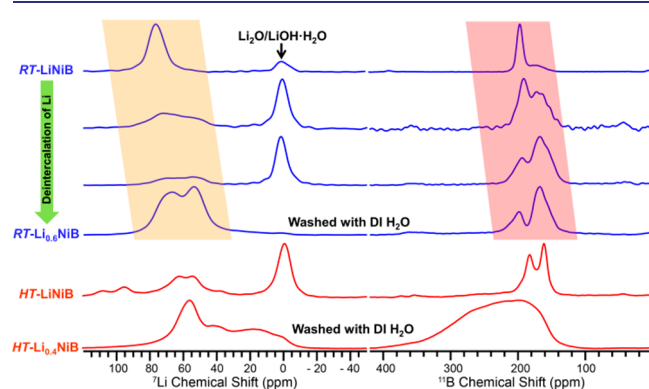


Figure 6. ⁷Li (left) and ¹¹B (right) solid-state NMR spectra showing the evolution of Li and B environment during deintercalation of *RT*-LiNiB (top) and *HT*-LiNiB (bottom). The peak at ~ 0 ppm in the ⁷Li spectra corresponds to a diamagnetic impurity, such as Li_2O , $\text{LiOH}\cdot\text{H}_2\text{O}$, or LiOH , which vanished completely after the sample was washed with deionized water.

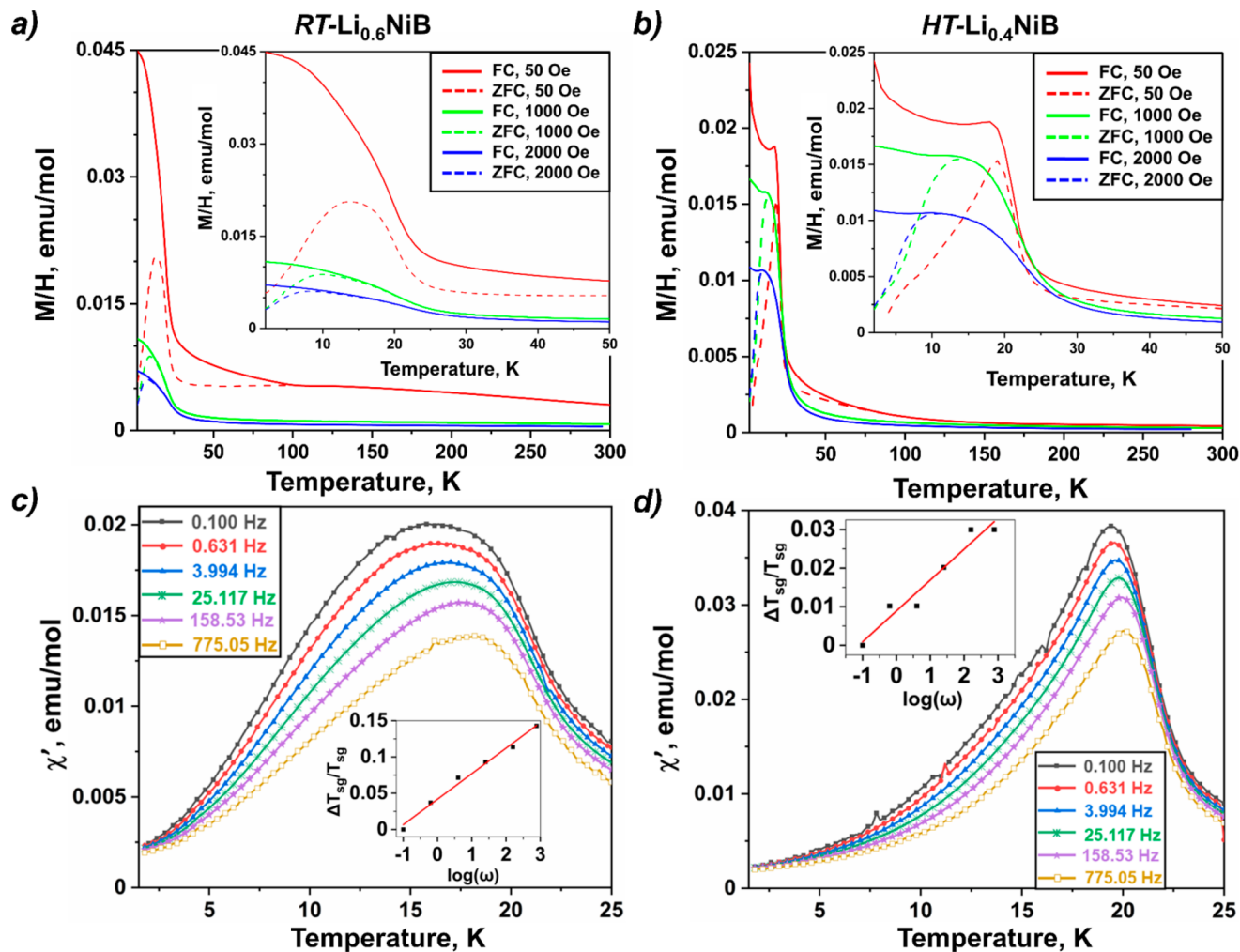


Figure 7. Temperature dependent susceptibility of polycrystalline samples of (a) $RT\text{-Li}_{0.6}\text{NiB}$ and (b) $HT\text{-Li}_{0.4}\text{NiB}$ in 2–300 K temperature range. Inset: temperature dependent susceptibility in 2–50 K temperature range. Temperature dependence of the real component of AC susceptibility, χ' , at different frequencies, ω , for (c) $RT\text{-Li}_{0.6}\text{NiB}$ and (d) $HT\text{-Li}_{0.4}\text{NiB}$. Inset: variation of spin glass temperature with frequency for the determination of Mydosh parameter.

$RT\text{-LiNiB}$ consists of two peaks, one of which (~ 70 – 80 ppm) corresponds to lithium in the structure⁴⁹ and the other one (~ 0 ppm) is due to a diamagnetic impurity, such as Li_2O , $\text{LiOH}\cdot\text{H}_2\text{O}$, or LiOH . During deintercalation driven by air exposure, the broad peak at ca. 70–80 ppm decreases in relative intensity and broadens, while the intensity of the peak at ~ 0 ppm rises, suggesting the increased content of lithium oxide upon deintercalation. Once the sample of $RT\text{-Li}_{0.6}\text{NiB}$ is washed with deionized water to remove LiOH , two broad peaks in the range of 40–80 ppm are observed in the MAS ^7Li NMR spectrum. These chemical shifts are in the range of typical ^7Li Knight shifts for Li-containing intermetallic compounds (28 ppm –125 ppm).⁵⁵ The two broad peaks are attributed to the superposition of multiple peaks corresponding to the slightly different Li environments in A, B, and C substructures found in $RT\text{-Li}_{0.6}\text{NiB}$. Similarly, one sharp peak for boron (~ 190 ppm) in the MAS ^{11}B NMR spectra of the parent compound $RT\text{-LiNiB}$ upon deintercalation broadens and splits into multiple peaks, corresponding to the superposition of slightly different B environments in $RT\text{-Li}_{0.6}\text{NiB}$ within single NiB, double $[\text{NiB}]_2$ or triple $[\text{NiB}]_3$ layers. The B chemical shifts in the range of 120 ppm–220 ppm are typical for metallic borides.⁵⁵

Upon Li deintercalation from the $HT\text{-LiNiB}$, Li and B environments change considerably, as is evident from the comparison of MAS ^7Li and ^{11}B NMR spectra for the parent $HT\text{-LiNiB}$ and $HT\text{-Li}_{0.4}\text{NiB}$. The ^7Li NMR spectrum of $HT\text{-LiNiB}$ consists of five peaks, four of which are in the range of ~ 40 – 115 ppm corresponding to lithium in the structure,⁴⁹ while the peak at ~ 0 ppm is a diamagnetic oxide/hydroxide impurity (Figure 6). Upon Li deintercalation and rinsing with deionized water to remove $\text{Li}_2\text{O}/\text{LiOH}$, the MAS ^7Li NMR spectrum of $HT\text{-Li}_{0.4}\text{NiB}$ feature multiple broad peaks in the range of ~ -10 to 80 ppm, indicating considerable disorder in $HT\text{-Li}_{0.4}\text{NiB}$ structure. Evidence of disorder is also clearly seen in the MAS ^{11}B NMR spectrum where two sharp peaks in the range of 120–200 ppm for the parent $HT\text{-LiNiB}$ compound are transformed to one broad peak (20–400 ppm range) in the $HT\text{-Li}_{0.4}\text{NiB}$ spectrum. The significant broadening of the ^{11}B solid-state NMR spectrum suggests a higher degree of disorder in $HT\text{-Li}_{0.4}\text{NiB}$ than $RT\text{-Li}_{0.6}\text{NiB}$, consistent with PDF, PXRD, and STEM data.

Magnetic Properties. Li deintercalation from RT - and $HT\text{-LiNiB}$ compounds alters their crystal structure significantly, as evident from STEM, X-ray PDF, DFT, and solid-state NMR. Upon deintercalation, the fraction of monatomic

[NiB] layers is condensed into doublets or triplets, which may lead to enhanced magnetic coupling between Ni spins. It was previously shown⁴⁹ that both *RT*-LiNiB and *HT*-LiNiB are temperature-independent paramagnets. Temperature- and field-dependence of magnetic susceptibility for *RT*-Li_{0.6}NiB and *HT*-Li_{0.4}NiB were measured to find out the effect of deintercalation of Li on the magnetic interactions between [NiB] layers (Figures 7, S19, S20). Both *RT*-Li_{0.6}NiB and *HT*-Li_{0.4}NiB are paramagnets at room temperature (with small amounts of ferromagnetic impurity phase, see below), but below 30 K, the magnetic transition emerges, manifesting in abrupt increase in molar magnetic susceptibility, χ , as well as in splitting of zero-field (ZFC) and field-cooled (FC) data (Figure 7a,b). The transition temperature or the temperature of ZFC/FC bifurcation shifts from ~14 to ~9 K with an increase in magnetic field from 1000 to 2000 Oe, while in the lower field of 50 Oe, the ZFC/FC splitting is evident already at ~90 K. The ZFC/FC splitting, as well as an apparent decrease of the characteristic temperature with increase in the magnetic field, are suggestive of the spin-glass-like, spin-cluster-like behavior or superparamagnetism.⁵⁶

To determine intrinsic molar magnetic susceptibility, χ , between 100 and 300 K, we corrected data for the ferromagnetic impurity by the Honda-Owen method,^{57,58} which also allowed an estimation of the impurity content (assumed to be Ni metal) to be 0.03 and 0.01 wt %, respectively, for *RT*-Li_{0.6}NiB and *HT*-Li_{0.4}NiB. The corrected data for $T > 100$ K were then fitted with the modified Curie-Weiss equation as $\chi = \chi_0 + C/(T - \theta)$ where $\chi_0 = 4.83(7) \times 10^{-5}$ emu mol⁻¹, $C = 9.2(2) \times 10^{-3}$ emu K mol⁻¹ and $\theta = 26(1)$ K for *RT*-Li_{0.6}NiB, and $\chi_0 = 6.06(4) \times 10^{-5}$ emu mol⁻¹, $C = 9.5(1) \times 10^{-3}$ emu K mol⁻¹ and $\theta = 35(1)$ K for *HT*-Li_{0.4}NiB (Figure S20, Table S7). For both compounds, temperature-independent contribution χ_0 is positive, consistent with the Pauli-paramagnetic (metallic) contribution being larger than the core-diamagnetic and Landau diamagnetic terms. The positive Weiss constant, θ , with low absolute value suggest a weak ferromagnetic coupling between Ni spins, whereas, from the value of C , the magnetic moment per Ni atom amounts to 0.28(1) μ_B .

The magnetization vs field (M vs H) plot (Figure S19) at temperatures above the transition is linear, except the low-field region due to the traces of ferromagnetic impurity. The linear dependence is consistent with the paramagnetic regime at $T > 100$ K. At 2 K, the magnetization displays a hysteresis loop; however, the full saturation is not attained even at the highest applied field of 7 T. We also note the considerably lower magnetization per Ni-atom at 7 T compared to the effective magnetic moment from Curie-Weiss fit.

The ZFC/FC splitting, lack of magnetization saturation, $M(H)$ hysteresis loop at 2 K, and lower magnetic moment from magnetization hints at the spin-glass-like or cluster-glass-like behavior. In spin- or cluster-glasses, the lack of long-range magnetic ordering is due to the frustration of the magnetically coupled spins due to a degree of randomness brought on by the structural disorder.^{56,59} To further confirm this, we have measured a frequency dependence of the real part of *ac*-susceptibility, χ' , and determined the Mydosh parameter, $\varphi = \Delta T_{SG}/[T_{SG} \times \log \omega]$, where T_{SG} is the temperature of the cusp, and ω is frequency.⁵⁶ The temperature of the cusp in χ' shifts to ward lower temperatures, and the extent of such shift is given by the Mydosh parameter, which is also a criterion for distinguishing canonical spin glasses from superparamagnets.

For canonical metallic spin glasses, the Mydosh parameter is in the range of 0.004–0.08. Both *RT*-Li_{0.6}NiB and *HT*-Li_{0.4}NiB have the frequency shift of the temperature cusp, and the Mydosh parameter was calculated to be 0.03 and 0.008, respectively (Figure 7c,d), suggesting the spin-glass behavior.

The change from temperature-independent *RT*- and *HT*-LiNiB paramagnets to spin-glass state in their deintercalated counterpart suggests that even partial Li deintercalation may induce magnetic coupling due to changes in spatial proximity of individual layers as well as electronic structure. Given the low magnetization per Ni-atom, we hypothesize that only Ni atoms within the tripled [NiB]₃ layers have interacting magnetic spins. This is supported by the overall scarcity of [NiB]₃ fragments in the structure (Figures 2, S6–S8) and their random distribution, which would be responsible for the observed spin-glass behavior. Stunningly similar behavior was recently reported for Cr₂TiC₂T_x (T_x is a surface termination group), which is the first experimentally confirmed example of a magnetic transition in an *MXene* material.⁵⁰ Similar to deintercalated LiNiB, deintercalation of Al from Pauli paramagnet Cr₂TiAlC₂ MAX phase results in a spin freezing transition at ~30 K. Below 30 K, a state with glassy spin dynamics in Cr₂TiC₂T_x is evidenced from ZFC-FC divergence and frequency dependence of the *ac*-susceptibility. The lack of long-range magnetic order resulting in a spin glassy state was hypothesized to be due to the inhomogeneous nature of the surface termination groups (T_x) or due to the flake-to-flake coupling of the randomly oriented flakes.

CONCLUSION

Synthesis of 2D MBene type [NiB] compounds was attempted from the LiNiB polymorphic compounds with alternating Li and [NiB] layers by the utilization of a *Chimie douce* (soft chemistry) approach. Complete removal of Li in this topochemical deintercalation process was not achieved; instead, the formation of novel metastable layered borides “Li_{~0.5}NiB” with reduced Li content was realized as evidenced by HAADF-STEM and ICP-MS analyses. The rate of deintercalation of Li depends on the exposure time (kinetics) as well as the type of environment. It was found that O₂ promoted the fastest deintercalation process. The unique structure of Li_{~0.5}NiB is best described as a random intergrowth of perfectly crystalline fragments of Li[NiB]_n (n = 1, 2, 3), retaining layered motives found in the parent compounds. Atomic resolution HAADF-STEM imaging clearly revealed that the deintercalation process follows a “zip-lock” mechanism: once the Li layer is removed, the “zip-lock” is closed, e.g., two or three [NiB] layers condense stabilizing the MBene type (NiB) phase. We also present an advanced approach for crystal structure determination by PDF-STEM-DFT synergistic combo applied for the deintercalated materials containing light elements (Li and B). Specifically, the developed methodology includes STEM for initial modeling of structural fragments, followed by iterative refinement of heavy Ni atomic coordinates from X-ray PDF and optimization of positions of the light elements (Li and B) by DFT. Such analysis provided conclusive evidence of the layered morphology for the *RT*-Li_{0.6}NiB and *HT*-Li_{0.4}NiB compounds in bulk and allowed for the determination of structural parameters as well as fractions of each substructure for Li[NiB]_n (n = 1, 2, 3). ⁷Li and ¹¹B solid state NMR spectroscopy not only provided evidence of the incomplete Li-deintercalation process but also indicated the change in the Li and B environments upon

deintercalation. Change in magnetic behavior from temperature independent paramagnetism to a spin glass state suggests that partial Li removal and condensation of monatomic [NiB] layers into [NiB]₂ or [NiB]₃ affect the electronic structure and induce magnetic interactions between Ni spins.

Li can be successfully deintercalated from LiNiB; however, single [NiB] layers are found to be unstable and further condense into [NiB]₂ and [NiB]₃. Comparisons to other 2D materials prepared via deintercalation, such as MXenes^{27–30,61} and germanane,^{4,62} suggest that surface termination with suitable reagents (-F, -Cl, -OH, -H, -CH₃) allows the stabilization of single-layer sheets. The finding of the appropriate terminating group for the LiNiB will not only allow for the preparation of an alluring family of MBenes (“NiBenes”) but also offer a way to study single layer sheets with various thickness, e.g., [NiB], [NiB]₂, and [NiB]₃. Further studies are underway to identify suitable terminating groups as well as reaction conditions.

■ ASSOCIATED CONTENT

§ Supporting Information

The Supporting Information is available free of charge at <https://pubs.acs.org/doi/10.1021/jacs.0c11397>.

Crystallographic data, Rietveld refinement plots, structure comparison, HAADF-STEM images, DOS diagrams ([PDF](#))

■ AUTHOR INFORMATION

Corresponding Author

Julia V. Zaikina – Department of Chemistry, Iowa State University, Ames, Iowa 50011, United States; orcid.org/0000-0002-8755-1926; Email: yzaikina@iastate.edu

Authors

Gourab Bhaskar – Department of Chemistry, Iowa State University, Ames, Iowa 50011, United States
Volodymyr Gvozdetskyi – Department of Chemistry, Iowa State University, Ames, Iowa 50011, United States
Maria Batuk – EMAT, Department of Physics, University of Antwerp, Antwerp 2020, Belgium; orcid.org/0000-0003-1411-9785
Kamila M. Wiaderek – Argonne National Laboratory, Lemont, Illinois 60439, United States
Yang Sun – Department of Applied Physics and Applied Mathematics, Columbia University, New York 10027, United States
Renhai Wang – Ames Laboratory, US DOE, Iowa State University, Ames, Iowa 50011, United States; Department of Physics, University of Science and Technology of China, Hefei 230026, China; orcid.org/0000-0003-4539-9273
Chao Zhang – Department of Physics, Yantai University, Yantai 264005, China; orcid.org/0000-0002-5957-2287
Scott L. Carnahan – Department of Chemistry and Ames Laboratory, US DOE, Iowa State University, Ames, Iowa 50011, United States

Xun Wu – Department of Chemistry and Ames Laboratory, US DOE, Iowa State University, Ames, Iowa 50011, United States

Raquel A. Ribeiro – Department of Physics and Astronomy, Iowa State University, Ames, Iowa 50011, United States

Sergey L. Bud'ko – Ames Laboratory, US DOE and Department of Physics and Astronomy, Iowa State University, Ames, Iowa 50011, United States

Paul C. Canfield – Ames Laboratory, US DOE and Department of Physics and Astronomy, Iowa State University, Ames, Iowa 50011, United States

Wenyu Huang – Department of Chemistry and Ames Laboratory, US DOE, Iowa State University, Ames, Iowa 50011, United States; orcid.org/0000-0003-2327-7259

Aaron J. Rossini – Department of Chemistry and Ames Laboratory, US DOE, Iowa State University, Ames, Iowa 50011, United States; orcid.org/0000-0002-1679-9203

Cai-Zhuang Wang – Ames Laboratory, US DOE and Department of Physics and Astronomy, Iowa State University, Ames, Iowa 50011, United States; orcid.org/0000-0002-0269-4785

Kai-Ming Ho – Department of Physics and Astronomy, Iowa State University, Ames, Iowa 50011, United States

Joke Hadermann – EMAT, Department of Physics, University of Antwerp, Antwerp 2020, Belgium; orcid.org/0000-0002-1756-2566

Complete contact information is available at:

<https://pubs.acs.org/10.1021/jacs.0c11397>

Author Contributions

The manuscript was written through contributions of all authors. All authors have given approval to the final version of the manuscript.

Notes

The authors declare no competing financial interest.

■ ACKNOWLEDGMENTS

Financial support from the National Science Foundation (DMR 1944551) CAREER award is gratefully acknowledged. A.J.R and S.L.C. (NMR spectroscopy), S.L.B. and P.C.C. (magnetism), X.W. and W.H. (ICP-MS) were supported by the US Department of Energy (DOE), Office of Science, Basic Energy Sciences, Materials Science and Engineering Division. R.A.R. was supported by the Gordon and Betty Moore Foundation's EPiQS Initiative through Grant GBMF4411. The Ames Laboratory is operated for the US Department of Energy by Iowa State University under contract #DE-AC02-07CH11358. R.W. and C.Z.W. were supported by the US Department of Energy (DOE), Office of Science, Basic Energy Sciences, Materials Science and Engineering Division, including a grant of computer time at the National Energy Research Scientific Computing Centre (NERSC) in Berkeley, CA. Y.S. was supported by NSF Awards No. EAR-1918134 and No. EAR-1918126. K.M.H. was supported by NSF Awards No. EAR-1918134. Use of the Advanced Photon Source at Argonne National Laboratory was supported by the U.S. Department of Energy, Office of Science, Office of Basic Energy Sciences, under Contract No. DE-AC02-06CH11357. We thank Ranjan Kumar Behera (Chemistry, Iowa State University) for the help with the ICP-MS data collection.

■ ABBREVIATIONS

PXRD, powder X-ray diffraction; X-ray PDF, X-ray Pair Distribution function; SEM, scanning electron microscopy; HAADF STEM, high angle annular dark field scanning transmission electron microscopy; EDXS, energy-dispersive X-ray spectroscopy; NMR, nuclear magnetic resonance; DFT,

density functional theory; ICP-MS, inductively couple plasma mass spectrometry

■ REFERENCES

- (1) Goodenough, J. B.; Park, K. S. The Li-Ion Rechargeable Battery: A Perspective. *J. Am. Chem. Soc.* **2013**, *135*, 1167–1176.
- (2) Yoshino, A. The Birth of the Lithium Ion Battery. *Angew. Chem., Int. Ed.* **2012**, *51*, 5798–5800.
- (3) Whittingham, M. S. Ultimate Limits to Intercalation Reactions for Lithium Batteries. *Chem. Rev.* **2014**, *114*, 11414–11443.
- (4) Bianco, E.; Butler, S.; Jiang, S.; Restrepo, O. D.; Windl, W.; Goldberger, J. E. Stability and Exfoliation of Germanane: A Germanium Graphene Analogue. *ACS Nano* **2013**, *7*, 4414–4421.
- (5) Butler, S. Z.; Hollen, S. M.; Cao, L.; Cui, Y.; Gupta, J. A.; Gutiérrez, H. R.; Heinz, T. F.; Hong, S. S.; Huang, J.; Ismach, A. F.; Halperin, E. J.; Kuno, M.; Plashnitsa, V. V.; Robinson, R. D.; Ruoff, R. S.; Salahuddin, S.; Shan, J.; Shi, L.; Spencer, M. G.; Terrones, M.; Windl, W.; Goldberger, J. E. Progress, challenges, and opportunities in two-dimensional materials beyond graphene. *ACS Nano* **2013**, *7*, 2898–2926.
- (6) Xiao, X.; Wang, H.; Urbankowski, P.; Gogotsi, Y. Topochemical synthesis of 2D materials. *Chem. Soc. Rev.* **2018**, *47*, 8744–8765.
- (7) Buha, J.; Manna, L. Solid State Intercalation, Deintercalation, and Cation Exchange in Colloidal 2D Bi_2Se_3 and Bi_2Te_3 Nanocrystals. *Chem. Mater.* **2017**, *29*, 1419–1429.
- (8) Cui, L.; Zhou, L.; Kang, Y. M.; An, Q. Recent Advances in the Rational Design and Synthesis of Two Dimensional Materials for Multivalent Ion Batteries. *ChemSusChem* **2020**, *13*, 1071.
- (9) Rodriguez, E. E.; Zavalij, P.; Hsieh, P. Y.; Green, M. A. Iodine as an Oxidant in the Topotactic Deintercalation of Interstitial Iron in Fe_{1+x}Te . *J. Am. Chem. Soc.* **2010**, *132*, 10006–10008.
- (10) Wang, M.; Dhahir, I. A.; Appiah, J.; Koski, K. J. Deintercalation of Zero-Valent Metals from Two-Dimensional Layered Chalcogenides. *Chem. Mater.* **2017**, *29*, 1650–1655.
- (11) Nakano, H.; Ikuno, T. Soft chemical synthesis of silicon nanosheets and their applications. *Appl. Phys. Rev.* **2016**, *3*, 040803.
- (12) Uppuluri, R.; Gupta, A. S.; Rosas, A. S.; Mallouk, T. E. Soft chemistry of ion-exchangeable layered metal oxides. *Chem. Soc. Rev.* **2018**, *47*, 2401–2430.
- (13) Rouxel, J.; Tournoux, M. Chimie douce with solid precursors, past and present. *Solid State Ionics* **1996**, *84*, 141–149.
- (14) Song, X.; Cheng, G.; Weber, D.; Pielenhofer, F.; Lei, S.; Klemenz, S.; Yeh, Y. W.; Filsinger, K. A.; Arnold, C. B.; Yao, N.; Schoop, L. M. Soft chemical synthesis of H_xCrS_2 : an antiferromagnetic material with alternating amorphous and crystalline layers. *J. Am. Chem. Soc.* **2019**, *141*, 15634–15640.
- (15) Murphy, D. W.; Cros, C.; DiSalvo, F. J.; Waszczak, J. V. Preparation and properties of Li_xVS_2 ($0 \leq x \leq 1$). *Inorg. Chem.* **1977**, *16*, 3027–3031.
- (16) Zhou, X.; Wilfong, B.; Vivanco, H.; Paglione, J.; Brown, C. M.; Rodriguez, E. E. Metastable Layered Cobalt Chalcogenides from Topochemical Deintercalation. *J. Am. Chem. Soc.* **2016**, *138*, 16432–16442.
- (17) Friederichs, G. M.; Schellenberg, I.; Pöttgen, R.; Duppel, V.; Kienle, L.; Günne auf der, J. S.; Johrendt, D. Metastable 11 K Superconductor $\text{Na}_{1-y}\text{Fe}_{2-x}\text{As}_2$. *Inorg. Chem.* **2012**, *51*, 8161–8167.
- (18) Todorov, I.; Chung, D. Y.; Claus, H.; Malliakas, C. D.; Douvalis, A. P.; Bakas, T.; He, J.; Dravid, V. P.; Kanatzidis, M. G. Topotactic redox chemistry of NaFeAs in Water and Air and superconducting behavior with stoichiometry change. *Chem. Mater.* **2010**, *22*, 3916–3925.
- (19) Gooch, M.; Lv, B.; Sasmal, K.; Tapp, J. H.; Tang, Z. J.; Guloy, A. M.; Lorenz, B.; Chu, C. W. Superconductivity in ternary iron pnictides: AFe_2As_2 (A = alkali metal) and LiFeAs . *Physica C* **2010**, *470*, 276–279.
- (20) Neilson, J. R.; McQueen, T. M. Bonding, Ion Mobility, and Rate-Limiting Steps in Deintercalation Reactions with ThCr_2Si_2 -type KNi_2Se_2 . *J. Am. Chem. Soc.* **2012**, *134*, 7750–7757.
- (21) Gruttner, A.; Nesper, R.; Schnering, H. G. V. Novel Metastable Germanium Modifications allo Ge and 4H Ge from $\text{Li}_7\text{Ge}_{12}$. *Angew. Chem., Int. Ed. Engl.* **1982**, *21*, 912–913.
- (22) Kiefer, F.; Karttunen, A. J.; Doblinger, M.; Fässler, T. F. Bulk synthesis and structure of a microcrystalline allotrope of germanium (m-allo-Ge). *Chem. Mater.* **2011**, *23*, 4578–4586.
- (23) Guloy, A. M.; Ramlau, R.; Tang, Z.; Schnelle, W.; Baitinger, M.; Grin, Y. A guest-free germanium clathrate. *Nature* **2006**, *443*, 320–323.
- (24) Zaikina, J. V.; Muthuswamy, E.; Lilova, K. I.; Gibbs, Z. M.; Zeilinger, M.; Snyder, G. J.; Fässler, T. F.; Navrotsky, A. N.; Kauzlarich, S. M. Thermochemistry, Morphology, and Optical Characterization of Germanium Allotropes. *Chem. Mater.* **2014**, *26*, 3263–3271.
- (25) Yamanaka, S.; Matsu-Ura, H.; Ishikawa, M. New deintercalation reaction of calcium from calcium disilicide. Synthesis of layered polysilane. *Mater. Res. Bull.* **1996**, *31*, 307–316.
- (26) Ryan, B. J.; Hanrahan, M. P.; Wang, Y.; Ramesh, U.; Nyamekye, C. K. A.; Nelson, R. D.; Liu, Z.; Huang, C.; Whitehead, B.; Wang, J.; Roling, R. D.; Smith, E. A.; Rossini, A. J.; Panthani, M. G. Silicene, Siloxene, or Silicane? Revealing the Structure and Optical Properties of Silicon Nanosheets Derived from Calcium Disilicide. *Chem. Mater.* **2020**, *32*, 795–804.
- (27) Gogotsi, Y.; Anasori, B. The Rise of MXenes. *ACS Nano* **2019**, *13*, 8491–8494.
- (28) Anasori, B.; Gogotsi, Y. *2D Metal Carbides and Nitrides (MXenes), Structure, Properties and Applications*; Springer: Berlin, 2019.
- (29) Naguib, M.; Kurtoglu, M.; Presser, V.; Lu, J.; Niu, J.; Heon, M.; Hultman, L.; Gogotsi, Y.; Barsoum, M. W. Two-Dimensional Nanocrystals Produced by Exfoliation of Ti_3AlC_2 . *Adv. Mater.* **2011**, *23*, 4248–4253.
- (30) Alhabeb, M.; Maleski, K.; Anasori, B.; Lelyukh, P.; Clark, L.; Sin, S.; Gogotsi, Y. Guidelines for synthesis and processing of two-dimensional titanium carbide ($\text{Ti}_3\text{C}_2\text{T}_x$ MXene). *Chem. Mater.* **2017**, *29*, 7633–7644.
- (31) Chen, W. Y.; Jiang, X.; Lai, S. N.; Peroulis, D.; Stanciu, L. Nanohybrids of a MXene and transition metal dichalcogenide for selective detection of volatile organic compounds. *Nat. Commun.* **2020**, *11*, 1302.
- (32) Zhang, Y. Z.; Wang, Y.; Jiang, Q.; El Demellawi, J. K.; Kim, H.; Alshareef, H. N. MXene Printing and Patterned Coating for Device Applications. *Adv. Mater.* **2020**, *32*, 1908486.
- (33) Rakhi, R. B.; Ahmed, B.; Hedhili, M. N.; Anjum, D. H.; Alshareef, H. N. Effect of Poststech Annealing Gas Composition on the Structural and Electrochemical Properties of Ti_2CT_x MXene Electrodes for Supercapacitor Applications. *Chem. Mater.* **2015**, *27*, 5314–5323.
- (34) Dong, Y.; Wu, Z. S.; Zheng, S.; Wang, X.; Qin, J.; Wang, S.; Shi, X.; Bao, X. Ti_3C_2 MXene-Derived Sodium/Potassium Titanate Nanoribbons for High-Performance Sodium/Potassium Ion Batteries with Enhanced Capacities. *ACS Nano* **2017**, *11*, 4792–4800.
- (35) Tang, Q.; Zhou, Z.; Shen, P. Are MXenes Promising Anode Materials for Li Ion Batteries? Computational Studies on Electronic Properties and Li Storage Capability of Ti_3C_2 and $\text{Ti}_3\text{C}_2\text{X}_2$ ($X = \text{F}, \text{OH}$) Monolayer. *J. Am. Chem. Soc.* **2012**, *134*, 16909–16916.
- (36) Er, D.; Li, J.; Naguib, M.; Gogotsi, Y.; Shenoy, V. B. Ti_3C_2 MXene as a High Capacity Electrode Material for Metal (Li, Na, K, Ca) Ion Batteries. *ACS Appl. Mater. Interfaces* **2014**, *6*, 11173–11179.
- (37) Naguib, M.; Come, J.; Dyatkin, B.; Presser, V.; Taberna, P. L.; Simon, P.; Barsoum, M. W.; Gogotsi, Y. MXene: a promising transition metal carbide anode for lithium-ion batteries. *Electrochim. Commun.* **2012**, *16*, 61–64.
- (38) Anasori, B.; Lukatskaya, M. R.; Gogotsi, Y. 2D metal carbides and nitrides (MXenes) for energy storage. *Nat. Rev. Mater.* **2017**, *2*, 16098.
- (39) Ma, Y.; Liu, N.; Li, L.; Hu, X.; Zou, Z.; Wang, J.; Luo, S.; Gao, Y. A highly flexible and sensitive piezoresistive sensor based on

- MXene with greatly changed interlayer distances. *Nat. Commun.* **2017**, *8*, 1207.
- (40) Zou, G.; Liu, B.; Guo, J.; Zhang, Q.; Fernandez, C.; Peng, Q. Synthesis of Nanoflower-Shaped MXene Derivative with Unexpected Catalytic Activity for Dehydrogenation of Sodium Alanates. *ACS Appl. Mater. Interfaces* **2017**, *9*, 7611–7618.
- (41) Wang, J.; Ye, T. N.; Gong, Y.; Wu, J.; Miao, N.; Tada, T.; Hosono, H. Discovery of hexagonal ternary phase Ti_2InB_2 and its evolution to layered boride TiB . *Nat. Commun.* **2019**, *10*, 2284.
- (42) Alameda, L. T.; Moradifar, P.; Metzger, Z. P.; Alem, N.; Schaak, R. E. Topochemical Deintercalation of Al from $MoAlB$: Stepwise Etching Pathway, Layered Intergrowth Structures, and Two-Dimensional MBene. *J. Am. Chem. Soc.* **2018**, *140*, 8833–8840.
- (43) Alameda, L. T.; Lord, R. W.; Barr, J. A.; Moradifar, P.; Metzger, Z. P.; Steimle, B. C.; Holder, C. F.; Alem, N.; Sinnott, S. B.; Schaak, R. E. Multi-Step Topochemical Pathway to Metastable Mo_2AlB_2 and Related Two-Dimensional Nanosheet Heterostructures. *J. Am. Chem. Soc.* **2019**, *141*, 10852–10861.
- (44) Yang, X.; Shang, C.; Zhou, S.; Zhao, J. MBenes: emerging 2D materials as efficient electrocatalysts for the nitrogen reduction reaction. *Nanoscale Horiz.* **2020**, *5*, 1106–1115.
- (45) Khazaei, M.; Wang, J.; Estili, M.; Ranjbar, A.; Suehara, S.; Arai, S.; Esfarjani, K.; Yunoki, S. Novel MAB phases and insights into their exfoliation into 2D MBenes. *Nanoscale* **2019**, *11*, 11305–11314.
- (46) Jiang, Z.; Wang, P.; Jiang, X.; Zhao, J. MBene (MnB): a new type of 2D metallic ferromagnet with high Curie temperature. *Nanoscale Horiz.* **2018**, *3*, 335–341.
- (47) Guo, Z.; Zhou, J.; Sun, Z. New two-dimensional transition metal borides for Li ion batteries and electrocatalysis. *J. Mater. Chem. A* **2017**, *5*, 23530–23535.
- (48) Bo, T.; Liu, P. F.; Zhang, J.; Wang, F.; Wang, B. T. Tetragonal and trigonal Mo_2B_2 monolayers: two new low-dimensional materials for Li-ion and Na-ion batteries. *Phys. Chem. Chem. Phys.* **2019**, *21*, 5178–5188.
- (49) Gvozdetskyi, V.; Bhaskar, G.; Batuk, M.; Zhao, X.; Wang, R.; Carnahan, S. L.; Hanrahan, M. P.; Ribeiro, R. A.; Canfield, P. C.; Rossini, A. J.; Wang, C. Z.; Ho, K. M.; Hadermann, J.; Zaikina, J. V. Computationally driven discovery of a family of layered $LiNiB$ polymorphs. *Angew. Chem., Int. Ed.* **2019**, *131*, 16002–16009.
- (50) Pohls, J. H.; Heyberger, M.; Mar, A. Comparison of computational and experimental inorganic crystal structures. *J. Solid State Chem.* **2020**, *290*, 121557.
- (51) Lugscheider, E.; Knotek, O.; Reimann, H. Das Dreistoffsystem Nickel-Chrom-Bor. *Monatsh. Chem.* **1974**, *105*, 80–90.
- (52) Billinge, S. J. L. The rise of the X-ray atomic pair distribution function method: a series of fortunate events. *Philos. Trans. R. Soc., A* **2019**, *377*, 20180413.
- (53) Tang, W.; Sanville, E.; Henkelman, G. A grid-based Bader analysis algorithm without lattice bias. *J. Phys.: Condens. Matter.* **2009**, *21*, 084204.
- (54) Sanville, E.; Kenny, S. D.; Smith, R.; Henkelman, G. An improved grid-based algorithm for Bader charge allocation. *J. Comput. Chem.* **2007**, *28*, 899–908.
- (55) Gvozdetskyi, V.; Hanrahan, M. P.; Ribeiro, R. A.; Kim, T. H.; Zhou, L.; Rossini, A. J.; Canfield, P. C.; Zaikina, J. V. A Hydride Route to Alkali Metal Borides: A Case Study of Lithium Nickel Borides. *Chem. - Eur. J.* **2019**, *25*, 4123–4135.
- (56) Mydosh, J. A. *Spin Glasses: An Experimental Introduction*; Taylor & Francis, London, 1993.
- (57) Honda, K. Die thermomagnetischen Eigenschaften der Elemente. *Ann. Phys.* **1910**, *337*, 1027–1063.
- (58) Owen, M. Magnetochemical Untersuchungen. Die thermomagnetischen Eigenschaften der Elemente. II. *Ann. Phys.* **1912**, *342*, 657–699.
- (59) Scholz, T.; Dronskowski, R. Spin-glass behavior of $Sn_{0.9}Fe_{3.1}N$: An experimental and quantum-theoretical study. *AIP Adv.* **2016**, *6*, 55107.
- (60) Hantanasirisakul, K.; Anasori, B.; Nemsak, S.; Hart, J. L.; Wu, J.; Yang, Y.; Chopdekar, R. V.; Shafer, P.; May, A. F.; Moon, E. J.; Zhou, J.; Zhang, Q.; Taheri, M. L.; May, S. J.; Gogotsi, Y. Evidence of a magnetic transition in atomically thin $Cr_2TiC_2T_x$ MXene. *Nanoscale Horiz.* **2020**, *5*, 1557–1565.
- (61) Hart, J. L.; Hantanasirisakul, K.; Lang, A. C.; Anasori, B.; Pinto, D.; Pivak, Y.; Tijn van Omme, J.; May, S. J.; Gogotsi, Y.; Taheri, M. L. Control of MXenes' electronic properties through termination and intercalation. *Nat. Commun.* **2019**, *10*, 522.
- (62) Jiang, S.; Butler, S.; Bianco, E.; Restrepo, O.; Windl, W.; Goldberger, J. E. Improving the stability and optoelectronic properties of germanane via one-step covalent methyl-termination. *Nat. Commun.* **2014**, *5*, 3389.